Transient Stability Analysis of Droop-Controlled Grid-Connected Converters With Inertia Emulating Low-Pass Filters

Pan, Donghua; Wang, Xiongfei; Liu, Fangcheng; Shi, Rongliang

Published in:
Proceedings of 2019 IEEE Energy Conversion Congress and Exposition (ECCE)

DOI (link to publication from Publisher):
10.1109/ECCE.2019.8912990

Publication date:
2019

Document Version
Accepted author manuscript, peer reviewed version

Transient Stability Analysis of Droop-Controlled Grid-Connected Converters With Inertia Emulating Low-Pass Filters

Donghua Pan
Dept. of Energy Technology
Aalborg University
Aalborg, Denmark
dop@et.aau.dk

Xiongfei Wang
Dept. of Energy Technology
Aalborg University
Aalborg, Denmark
xwa@et.aau.dk

Fangcheng Liu
Central Research Institute
Huawei Technologies Co., Ltd.
Shanghai, China
formula.liu@huawei.com

Rongliang Shi
Central Research Institute
Huawei Technologies Co., Ltd.
Shanghai, China
shirongliang@huawei.com

***Abstract*—This paper presents a design-oriented transient stability analysis of a droop-controlled voltage-source converter (VSC), where the low-pass filters (LPFs) for inertia emulating are in focus. It reveals that the two LPFs in the active and reactive power loops take opposite effects on the transient stability: the former degrades the stability while the latter improves it. By means of the phase portrait, the mechanism behind this is explicitly elaborated, and the quantitative impacts of the inertia emulating terms are clearly identified. Subsequently, a design guideline of the LPFs for enhancing the transient stability is proposed. Finally, experimental results are provided to verify the theoretical analysis.**

***Index Terms*—Droop control, large-signal disturbance, transient stability, virtual inertia, voltage-source converter.**

I. Introduction

Voltage-source converters (VSCs) are widely used in modern power grids for renewable energy generations and energy-saving applications [1]–[4]. To regulate the exchange of active and reactive powers with the grid, the *P-f* and *Q-V* droop control is usually employed in the VSCs [5], [6]. In the droop controller, low-pass filters (LPFs) are usually introduced to mimic the inertial characteristic of a synchronous generator [7], [8]. Thus, like the synchronous generator, the droop-controlled VSCs will also suffer from the stability problem under a grid disturbance.

Substantial research efforts have been devoted to the stability analysis of the droop-controlled VSC, with the main focus on the small-signal disturbance [9], [10]. However, if a large- signal disturbance happens, e.g., a fault on transmission lines, a severe grid voltage sag, and a large load swing, the *transient stability* of the VSC, which characterizes the ability of the VSC to maintain synchronization with the grid [11], is concerned, and it attracts increasing research interests recently. In [12] and [13], a transient instability phenomenon of the droop-controlled VSC is found in the case of a current saturation due to a grid voltage sag. The similar phenomenon is also predicted in [14] by means of the deep learning theory. In [15], a VSC with the power-synchronization control (an equivalence to the droop control [16], [17]) is studied, and its transient behavior is explored in different types of grid faults. Nevertheless, a clear consensus regarding the role of inertial terms (or the LPFs) in the transient response is still missing.

This paper aims to address this issue by quantifying the impact of the inertia emulating LPFs on the transient behavior of the droop-controlled VSC. To begin with, a large-signal model of the droop controller, which accounts for the cross coupling between the active and reactive power loops, is developed in Section II. Based on this model, an in-depth transient stability analysis is carried out by means of the phase portrait in Section III. It is shown that the LPF in active power loop degrades the transient stability while the LPF in reactive power loop improves it. To acquire a superior stability, a fast LPF with a high cutoff frequency (a low inertia) has to be preserved for the active power loop. Yet, for the reactive power loop, a slow LPF with a low cutoff frequency is critical to alleviate the undesired transient voltage drop caused by the reactive power control. These theoretical expectations are confirmed by experimental results in Section IV, before drawing the conclusion in Section V.

II. Large-Signal Modeling of Droop-Controlled VSC

Fig. 1 shows a single-line diagram of a three-phase VSC connecting to the grid. A constant dc voltage V_{in} is assumed at the input of the VSC. Inductor L_f and capacitor C_f form an output filter of the VSC, which is actually an *LCL* filter considering the grid inductance L_g at the point of common coupling (PCC) [18]–[20]. The grid voltage is represented by a vector **E** which has an amplitude E and a frequency ω_0.

The VSC is controlled as a grid-forming voltage source by the well-known *P-f* and *Q-V* droop method [5], [6]. Moreover, to mitigate power fluctuations caused by the load unbalance, LPFs are added into the power control loops [9], [10]. In this way, control laws can be written as

$$\omega = \omega_0 + K_p \cdot \frac{\omega_p}{s+\omega_p} \cdot \left(P_0 - P\right) \tag{1}$$

$$V = V_0 + K_q \cdot \frac{\omega_q}{s+\omega_q} \cdot \left(Q_0 - Q\right) \tag{2}$$

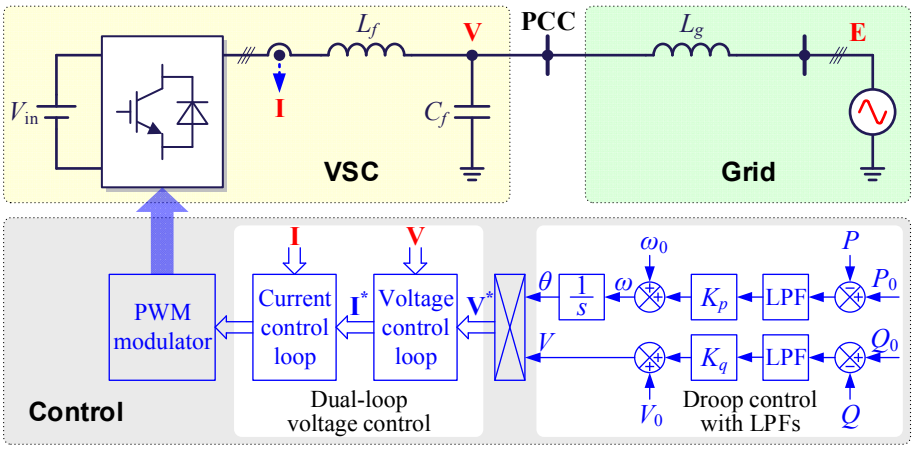

Fig. 1. Configuration of a droop-controlled VSC connected to the grid.

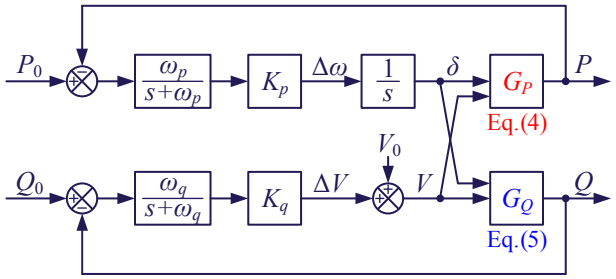

Fig. 2. Large-signal model of the power control loops.

where ω and V are the frequency and amplitude of the VSC output voltage, with ω_0 and V_0 being their references; P and Q are the active and reactive powers, with P_0 and Q_0 being their references; K_p and K_q are the P-f and Q-V droop gains; and ω_p and ω_q are the LPF cutoff frequencies in the active and reactive power loops, respectively.

Except for power filtering, the use of LPFs introduces a virtual inertia J to the VSC, which has been proved as [7], [8]

$$J = \frac{1}{K_p \omega_p}. \tag{3}$$

Thus, a large ω_p leads to a smaller inertia J.

As shown in Fig. 1, ω is processed by a pure integrator to obtain the phase θ, which together with V, generates the voltage reference vector $\mathbf{V}^*$. The output voltage vector $\mathbf{V}$ is regulated by a voltage loop to track this reference. A current loop is cascaded to the voltage loop to damp the LC resonance and thus enhance the system stability [9], [10]. Generally, the dynamic of the outer power loop is over a decade slower than that of the inner voltage & current loop [21]. The outer loop and the inner loop can thus be evaluated individually. Hence, when analyzing the transient stability issue caused by the outer power loop, the inner dual-loop voltage control can be regarded as a unity gain with an ideal reference tracking [12]–[15], i.e., $\mathbf{V} = \mathbf{V}^*$ and $|\mathbf{V}| = V$.

Taking the voltage vector $\mathbf{E}$ as a reference and assuming the phase difference between $\mathbf{V}$ and $\mathbf{E}$ is δ, i.e., the power angle, we can obtain $\mathbf{E} = E\angle 0$ and $\mathbf{V} = V\angle\delta$. Thus, P and Q from the PCC can be expressed as [11]

$$P = \frac{3}{2}\cdot\frac{EV\sin\delta}{X_g} \tag{4}$$

$$Q = \frac{3}{2}\cdot\frac{V^2 - EV\cos\delta}{X_g}. \tag{5}$$

Obviously, both P and Q are related to δ and V, which means that the active power loop that commands δ and the reactive power loop that commands V are coupled with each other. Considering this crossing coupling, a large-signal model of the power control loop is obtained as Fig. 2, where G_P and G_Q are the expressions of P and Q, i.e., (4) and (5), respectively.

III. Transient Stability of Droop-Controlled VSC

Generally, the transient stability of the VSC is dependent on the dynamic response of δ under a large disturbance. Due to the crossing-coupling effect, the dynamic performance of δ is determined by the active and reactive power loops together, where their LPFs play an important role. To show the impacts of two LPFs individually, the droop controller without an LPF in the reactive power loop is discussed first.

A. Effect of LPF in Active Power Loop

Recalling (4) and Fig. 2, the dynamic equation of δ, with an LPF in the active power loop, can be described as

$$\begin{aligned} \delta &= \frac{K_p}{s}\cdot\frac{\omega_p}{s+\omega_p}\cdot\left(P_0 - \frac{3}{2}\cdot\frac{EV\sin\delta}{X_g}\right) \\ \Rightarrow\ \ddot{\delta} &= -\omega_p\dot{\delta} + \omega_p K_p\left(P_0 - \frac{3}{2}\cdot\frac{EV\sin\delta}{X_g}\right) \end{aligned} \tag{6}$$

From (6), it is implicit to tell the dynamic response of δ, since it is coupled with the other controlled variable V, which is commanded by the reactive power loop. To quantify this coupling effect, we first rewrite the Q-V droop law by substituting (5) into (2) and letting $\omega_q = \infty$ (no LPF in the reactive power loop), i.e.,

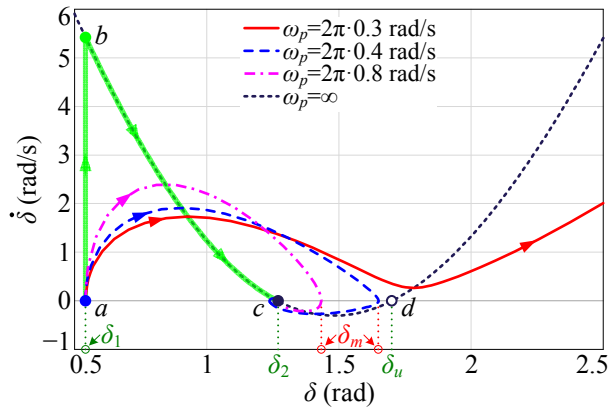

Fig. 3. Phase portraits of the droop control with an LPF in active power loop (E = 1 p.u. → 0.6 p.u. and $\omega_q = \infty$).

$$V = V_0 + K_{\text{qv}}\left(Q_0 - \frac{3}{2}\cdot\frac{V^2 - EV\cos\delta}{X_g}\right) \tag{7}$$

which is obviously a quadratic equation of V. Solving this equation, V is found related to δ by (8). Substituting (8) into (6), the dynamic equation of δ, considering the effect of reactive power control, can be obtained as (9) (see the bottom of this page), which is a second-order differential equation solely related to δ.

Hence, the dynamic response of δ can be explicitly judged by (9), which is critical for the transient stability analysis. However, due to the high nonlinearity, it is difficult to acquire an analytical solution of (9). In contrast, a graphical evaluation of (9) can be easily carried out by the $\dot{\delta}$-δ curve, which is the so-called phase portrait [22]. Based on the phase portrait, the change of δ can be readily predicted, i.e., δ will increase if $\dot{\delta} > 0$ and decrease if $\dot{\delta} < 0$, and $\dot{\delta} = 0$ corresponds to equilibrium points. According to parameters in Table I, the phase portraits during the grid fault with a voltage sag are plotted in Fig. 3, where the curve with $\omega_p = \infty$ (no LPF in the active power loop and thus no inertia) is provided as a reference. It is worth noting that for $\omega_p = \infty$, the second-order differential equation in (9) will be reduced to a first-order one.

Before the fault, i.e., E = 1 p.u., the VSC operates at point a with a power angle of δ_1. When E drops to 0.6 p.u., δ may go to a new equilibrium or diverge to infinite, depending on ω_p. For $\omega_p = \infty$, there are two equilibrium points, where point c (the solid dot) is the stable one, since δ can return to this point irrespective of a small disturbance; while point d (the open circle) is the unstable one, since a small disturbance will force δ to departure from this point. When the grid voltage sag occurs, the operating point jumps from a to b and then moves toward c, shown as the trajectory with arrows in Fig. 3. Once reaching point c, a new steady state is achieved due to $\dot{\delta} = 0$, and δ will stop at δ_2 and never exceed it. This implies a transient response with no *overshoot*, which essentially results from the first-order dynamic behavior.

With a finite ω_p, the system will behave in a second-order manner. Although the operating point still moves from a to c in a stable operation, the trajectory is different from $\omega_p = \infty$. During the transient response, δ can exceed its steady-state value δ_2, which implies an overshoot in the power angle. For example, if $\omega_p = 2\pi\cdot0.4$ rad/s, δ starts to increase from δ_1 due to $\dot{\delta} > 0$, and reaches its maximum value δ_m when $\dot{\delta}$ first falls down to 0, then declines due to $\dot{\delta} < 0$ until terminating at δ_2. The difference between δ_m and δ_2 is defined as the power angle overshoot. It is known that for a stable operation, δ_m should not exceed δ_u, i.e., the power angle at the unstable equilibrium point (point d) [11]. To meet this requirement, a smaller overshoot would be desirable.

As shown in Fig. 3, when ω_p is increased to $2\pi\cdot0.8$ rad/s, a smaller δ_m (namely a smaller overshoot) is yielded. Hence, a large ω_p is expected to reduce the power angle overshoot and thus to enhance the transient stability, and $\omega_p = \infty$ is the best because of no overshoot. On the contrary, an instability can arise with a small ω_p. For example, when ω_p is reduced to $2\pi\cdot0.3$ rad/s, δ exceeds δ_u and then keeps increasing as $\dot{\delta} > 0$ always holds, which means a loss of synchronization (LoS).

Recalling the equivalence derived in (3), the inertia J is inversely proportional to ω_p. Thus, a small inertia is critical to improve the transient stability, and no inertia is the best case. This finding provides a new perspective on the virtual inertia: while the virtual inertia improves the system frequency stability [23], it degrades the transient stability by raising the system control order and should be taken with great caution.

B. Effect of LPF in Reactive Power Loop

Based on the above analysis, the impact of LPF in the reactive power loop is further investigated. With the LPF, the dynamic equation of the reactive power loop is changed into

$$\begin{aligned} V &= V_0 + K_q\cdot\frac{\omega_q}{s+\omega_q}\cdot\left(Q_0 - \frac{3}{2}\cdot\frac{V^2 - EV\cos\delta}{X_g}\right) \\ \Rightarrow\ \dot{V} &= -\omega_q V + \omega_q V_0 + \omega_q K_q\left(Q_0 - \frac{3}{2}\cdot\frac{V^2 - EV\cos\delta}{X_g}\right) \end{aligned} \tag{10}$$

$$V = \frac{1.5K_{\text{qv}}E\cos\delta - X_g + \sqrt{\left(X_g - 1.5K_{\text{qv}}E\cos\delta\right)^2 + 6K_{\text{qv}}X_g\left(V_0 + K_{\text{qv}}Q_0\right)}}{3K_{\text{qv}}}. \tag{8}$$

$$\ddot{\delta} = -\omega_p\dot{\delta} + \omega_p K_p\left(P_0 - \frac{3}{2}\cdot\frac{E\sin\delta}{X_g}\cdot\frac{1.5K_qE\cos\delta - X_g + \sqrt{\left(X_g - 1.5K_qE\cos\delta\right)^2 + 6K_qX_g\left(V_0 + K_qQ_0\right)}}{3K_q}\right). \tag{9}$$

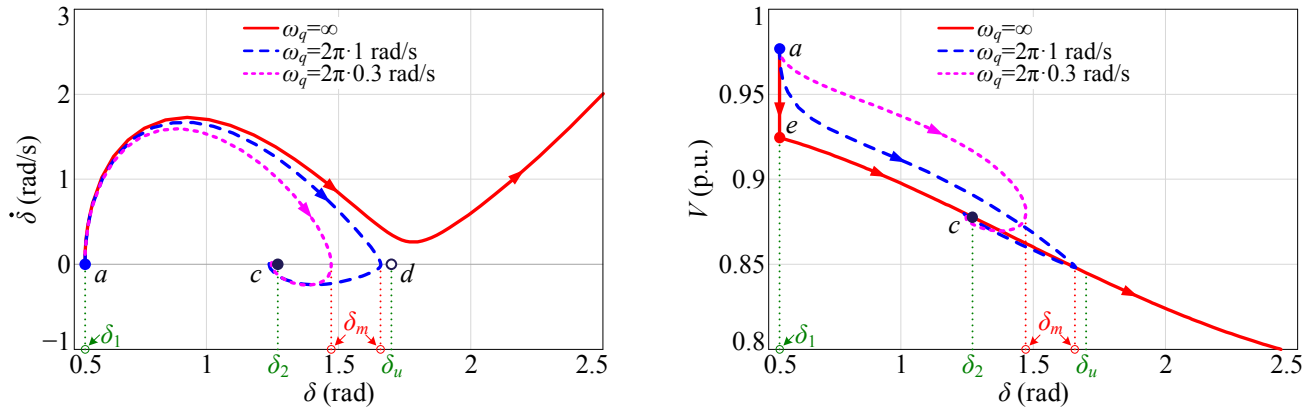

(a) (b)

Fig. 4. (a) Phase portraits and (b) V-δ curves of the droop control with LPFs in both active and reactive power loops (E = 1 p.u. → 0.6 p.u. and $\omega_p = 2\pi \cdot 0.3$ rad/s).

Unlike the quadratic equation in (7), (10) is a differential equation. It is thus difficult to acquire an explicit expression of V [like (8)] from this differential equation. Fortunately, we can use the MATLAB command "ode45" to solve the differential equations in (6) and (10) together, and then plot the phase portraits and the V-δ curves, as shown in Fig. 4. $\omega_p = 2\pi \cdot 0.3$ rad/s is fixed in this study, and the unstable responses without the LPF ($\omega_q = \infty$) are redrawn with the solid lines for comparison. By adding the LPF (a finite ω_q), the system trajectory converges to the equilibrium point c, implying a restoration of synchronization (RoS). Moreover, as ω_q goes lower, the system trajectory is shifted inward with a smaller power angle overshoot, as shown with the dashed lines in Fig. 4(a). Hence, a smaller ω_q leads to a better transient stability.

To reveal the underlying mechanism, the VSC voltage dynamic, which is dominated by the reactive power loop, is further analyzed with the V-δ curves shown in Fig. 4(b). For $\omega_q = \infty$ (no LPF), as E drops suddenly at the fault occurring instant, Q increases sharply referring to (5), which causes V to jump down from point a to point e. Then, as δ increases, Q also increases according to (5), which causes V to drop continuously following the Q-V droop law. This transient voltage drop will reduce P referring to (4), which, in turn, enlarges $\dot{\delta}$ and pushes δ to the stability boundary δ_u. As a result, the transient stability is weaken. Such a negative effect is alleviated by the LPF, which slows down the dynamic response of the reactive power loop and makes V insensitive to the variation of Q. Hence, during the transient process, the VSC voltage is raised with the decrease of ω_q, as shown with the dashed lines in Fig. 4(b). The raised V helps to increase P and push δ lower than δ_u, which means a RoS. Accordingly, V declines slowly from point a and finally stops at point c.

From the above analysis, it can be concluded that the two LPFs in the active and reactive power loops take opposite effects on the transient stability: the former degrades the stability while the latter improves it. The strong transient stability demands a fast LPF with a high cutoff frequency (a low inertia) in the active power loop and a slow LPF with a low cutoff frequency in the reactive power loop.

IV. Experimental Results

To verify the theoretical analysis, an experimental setup, as shown in Fig. 5, is built and test in the lab. The VSC is implemented by a Danfoss VLT FC-103P11K inverter, whose input is supplied by a constant dc voltage source, and its output is connected with an LC filter. A three-phase inductor is used to emulate the grid impedance X_g. The Chroma 61845 grid simulator is employed to provide the grid voltage **E**. The VSC output voltage **V** and VSC output current **I** are measured through the dSPACE DS2004 A/D board. The measured signals are sent to the dSPACE DS1007 platform to implement the outer power control and the inner dual-loop voltage control. The phase angles of **V** and **E** are measured by a fast phase-locked loop, and their phase difference, which is denoted as the power angle δ, is fed to the oscilloscope through the dSPACE DS2102 D/A board.

Table I gives the nominal parameters of the experimental setup. A low grid voltage E = 100 V is intentionally chosen for the convenience of emulating the low short-circuit-ratio grid condition. The droop gains K_p and K_q are designed according to the allowed frequency deviation $\Delta\omega$ under the maximum active power $P_{\max}$ and the allowed voltage deviation ΔV under the maximum reactive power $Q_{\max}$, respectively [5], [6]. For the grid-connected application, the VSC can inject the full active power or the full reactive power depending on the operating scenarios. Hence, $P_{\max} = Q_{\max} = 1$ p.u.. Meanwhile, $\Delta\omega = 0.04\omega_0$ and $\Delta V = 0.1V_0$ are set, which give rise to $K_p = 0.04\omega_0/P_{\max}$ and $K_q = 0.1V_0/Q_{\max}$, respectively.

To perform a comparative test, different sets of controller parameters are examined, and they are grouped into three cases, as shown in Table II. Case I, Case II, and Case III refer to 1) the droop control without LPFs (no inertia), 2) the droop control with an LPF in active power loop, and 3) the droop control with LPFs in both active and reactive power loops, respectively. Based on these parameters, transient responses of the VSC are examined in the case of the grid voltage sag from 1 p.u. to 0.6 p.u..

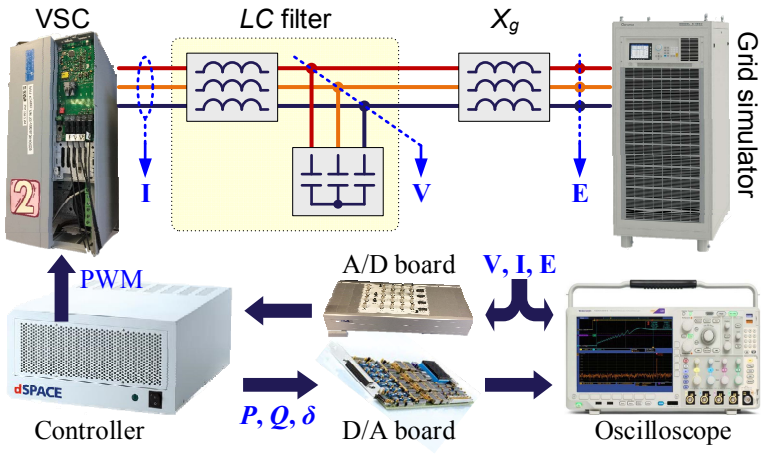

Fig. 5. Configuration of the experimental setup.

TABLE I. NOMINAL PARAMETERS OF THE EXPERIMENTAL SETUP

Parameter	Value	p.u.	Parameter	Value	p.u.
Rated active power P_0	2 kW	1.0	Rated reactive power Q_0	0	0
Rated voltage V_0	100 V	1.0	Filter inductance L_f	1.5 mH	0.06
Grid voltage E	100 V	1.0	Filter capacitance C_f	20 μF	0.05
Grid frequency ω_0	314 rad/s		Grid inductance L_g	12 mH	0.5
P-f droop gain K_p	$0.04\omega_0/P_{max}$	0.04	Q-V droop gain K_q	$0.1V_0/Q_{max}$	0.1

TABLE II. CONTROLLER PARAMETERS FOR THE EXPERIMENTAL TEST

Parm	Case I	Case II-A	Case II-B	Case II-C	Case III-A	Case III-B
ω_p	∞	$2\pi\cdot0.4$rad/s	$2\pi\cdot0.8$rad/s	$2\pi\cdot0.3$rad/s	$2\pi\cdot0.3$rad/s	$2\pi\cdot0.3$rad/s
ω_q	∞	∞	∞	∞	$2\pi\cdot1$rad/s	$2\pi\cdot0.3$rad/s

Fig. 6 shows experimental results acquired with the controller parameters in Case I and Case II. For Case I, $\omega_p = \omega_q = \infty$, no inertia is preserved, and the control system is reduce to a first-order one. As shown in Fig. 6(a), when E drops to 0.6 p.u., δ starts to increase gradually and reaches a new steady state without any overshoot, which confirms a first-order dynamic behavior and implies a strong transient stability. The power angles before and after the fault are 30º and 70º, respectively, which correspond to δ_1 and δ_2 in Fig. 3. For Case II, the LPF in active power loop is enabled with three different ω_p, while $\omega_q = \infty$ remains. With $\omega_p = 2\pi\cdot0.4$ rad/s (Case II-A) and $\omega_p = 2\pi\cdot0.8$ rad/s (Case II-B), power angle overshoots are observed in their transient responses, where δ increases to its maximum value δ_m first and then declines to the steady-state δ_2, as shown in Figs. 6(b) and 6(c). These verify a second-order dynamic response as expected in Section III-A. $\delta_m = 95º$ and $\delta_m = 84º$ are measured in the two cases, which proves a decreased overshoot with the increase of ω_p. On the contrary, if ω_p is reduced to $2\pi\cdot0.3$ rad/s (Case II-C), as shown in Fig. 6(d), low-frequency oscillations are triggered in the waveforms of P, Q, δ, V, and I, which imply a LoS and agree with the analysis in Section III-A.

Such an instability can be removed by incorporating a slow LPF into the reactive power loop, as illustrated in Section III-B. For verification, $\omega_q = 2\pi\cdot1$ rad/s (Case III-A) and $\omega_q = 2\pi\cdot0.3$ rad/s (Case III-B) are tested on the basis of $\omega_p = 2\pi\cdot0.3$ rad/s, as shown in Figs. 7(a) and 7(b). It can be seen that as ω_q decreases, V is raised during the transient process, which thus helps to reduce the power angle overshoot. Consequently, $\delta_m = 95º$ and $\delta_m = 86º$ are measured in the two cases. These experimental results confirm the theoretical analysis in Section III-B.

V. CONCLUSIONS

This paper has explored the transient stability of the droop-controlled VSC by considering the inertia emulating LPFs. A large-signal model considering the coupling effect has been developed to characterize the nonlinear transient responses. Based on this model, an in-depth transient stability analysis is performed using the phase portrait to quantify the impacts of LPFs. It has been shown that the LPF in active power loop degrades the transient stability while the LPF in reactive power loop improves it. As a result, a fast LPF with a high cutoff frequency (a low inertia) has to be preserved for the active power loop to ensure a strong stability. Yet, for the reactive power loop, a slow LPF with a low cutoff frequency is critical to alleviate the undesired transient voltage drop caused by the reactive power control. The theoretical findings have been verified by experimental results.

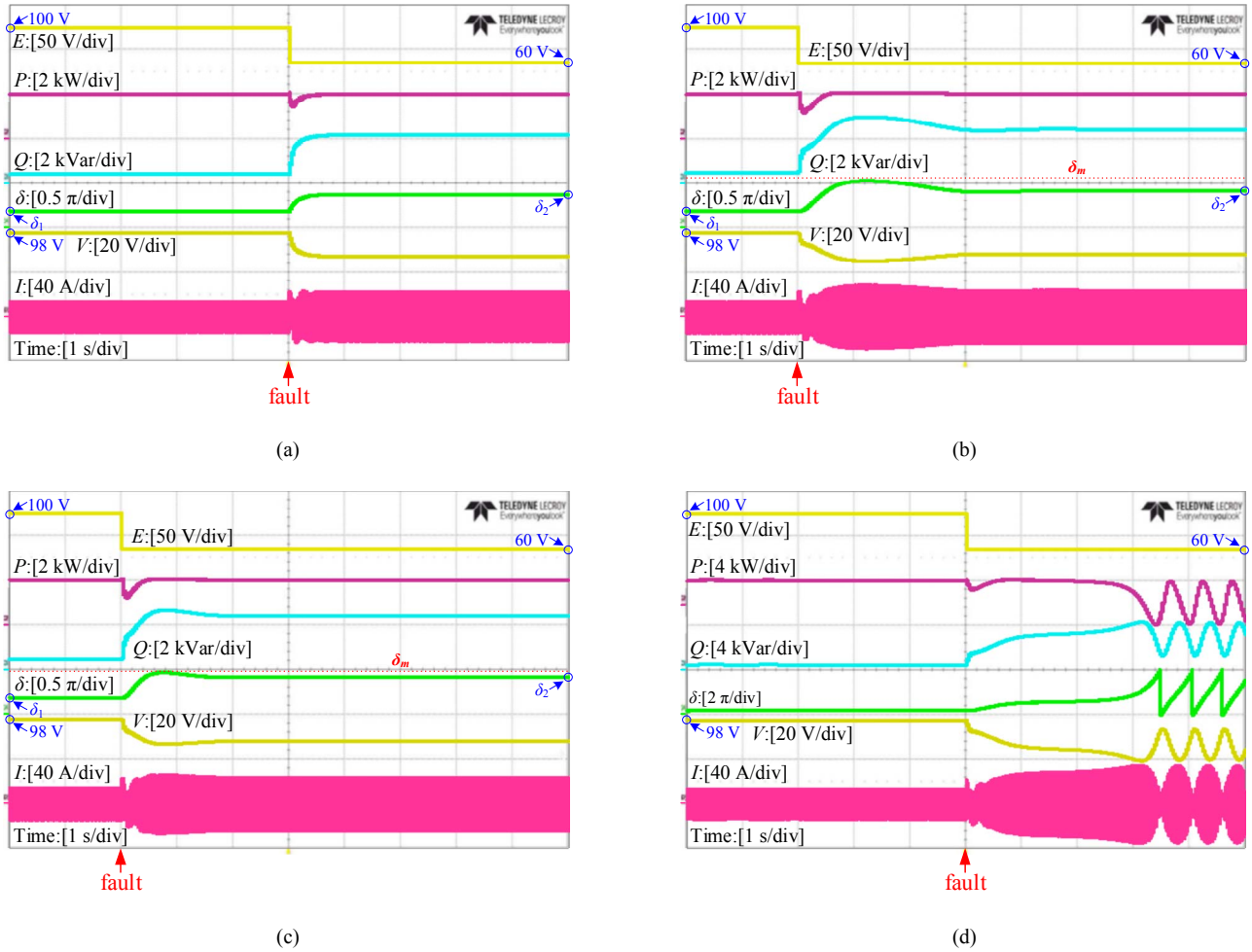

Fig. 6. Experimental transient responses of the droop-controlled VSC with controller parameters in Case I and Case II. (a) Case I: $\omega_p = \omega_q = \infty$. (b) Case II-A: $\omega_p = 2\pi \cdot 0.4$ rad/s and $\omega_q = \infty$. (c) Case II-B: $\omega_p = 2\pi \cdot 0.8$ rad/s and $\omega_q = \infty$. (d) Case II-C: $\omega_p = 2\pi \cdot 0.3$ rad/s and $\omega_q = \infty$.

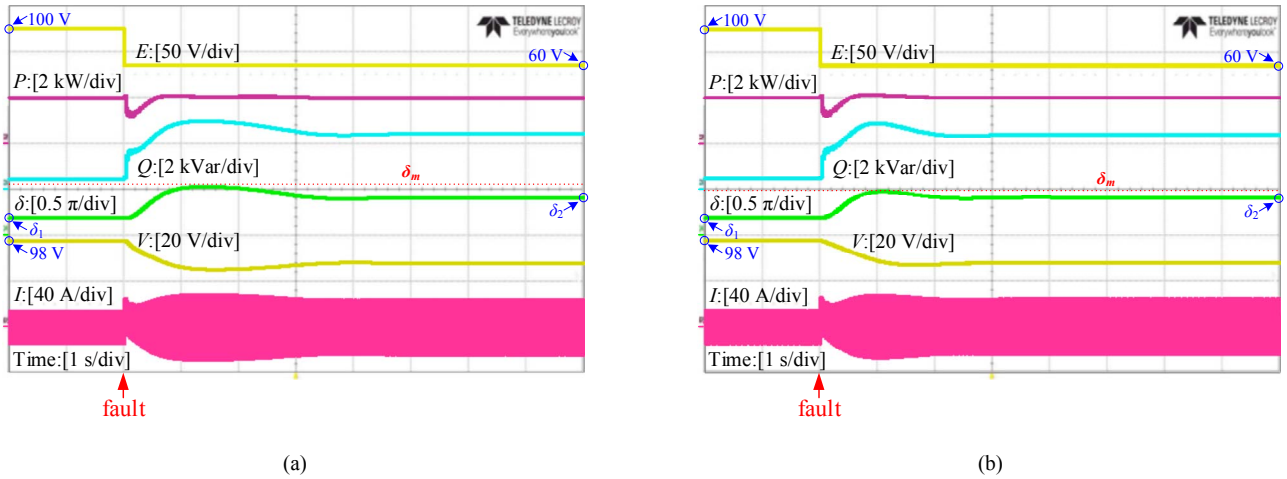

Fig. 7. Experimental transient responses of the droop-controlled VSC with controller parameters in Case III. (a) Case III-A: $\omega_p = 2\pi \cdot 0.3$ rad/s and $\omega_q = 2\pi \cdot 1$ rad/s. (b) Case III-B: $\omega_p = 2\pi \cdot 0.3$ rad/s and $\omega_q = 2\pi \cdot 0.3$ rad/s.

REFERENCES

[1] J. Rocabert, A. Luna, F. Blaabjerg, and P. Rodríguez, "Control of power converters in AC microgrids," *IEEE Trans. Power Electron.*, vol. 27, no. 11, pp. 4734−4749, Nov. 2012.

[2] D. Pan, X. Ruan, C. Bao, W. Li, and X. Wang, "Capacitor-current-feedback active damping with reduced computation delay for improving robustness of *LCL*-type grid-connected inverter," *IEEE Trans. Power Electron.*, vol. 29, no. 7, pp. 3414−3427, Jul. 2014.

[3] D. Pan, X. Ruan, C. Bao, W. Li, and X. Wang, "Optimized controller design for *LCL*-type grid-connected inverter to achieve high robustness against grid-impedance variation," *IEEE Trans. Ind. Electron.*, vol. 62, no. 3, pp. 1537−1547, Mar. 2015.

[4] D. Pan, X. Ruan, X. Wang, H. Yu, and Z. Xing, "Analysis and design of current control schemes for *LCL*-type grid-connected inverter based on a general mathematical model," *IEEE Trans. Power Electron.*, vol. 32, no. 6, pp. 4395−4410, Jun. 2017.

[5] Y. W. Li, D. M. Vilathgamuwa, and P. C. Loh, "Design, analysis, and real-time testing of a controller for multibus microgrid system," *IEEE Trans. Power Electron.*, vol. 19, no. 5, pp. 1195−1204, Sep. 2004.

[6] Y. W. Li and C.-N. Kao, "An accurate power control strategy for power-electronics-interfaced distributed generation units operating in a low-voltage multibus microgrid," *IEEE Trans. Power Electron.*, vol. 24, no. 12, pp. 2977−2988, Dec. 2009.

[7] S. D'Arco and J. A. Suul, "Equivalence of virtual synchronous machines and frequency-droops for converter-based microgrids," *IEEE Trans. Smart Grid*, vol. 5, no. 1, pp. 394−395, Jan. 2014.

[8] J. Liu, Y. Miura, and T. Ise, "Comparison of dynamic characteristics between virtual synchronous generator and droop control in inverter-based distributed generators," *IEEE Trans. Power Electron.*, vol. 31, no. 5, pp. 3600−3611, May 2016.

[9] E. A. A. Coelho, P. C. Cortizo, and P. F. D. Garcia, "Small-signal stability for parallel-connected inverters in stand-alone AC supply systems," *IEEE Trans. Ind. Appl.*, vol. 38, no. 2, pp. 533−542, Mar./Apr. 2002.

[10] N. Pogaku, M. Prodanović, and T. C. Green, "Modeling, analysis and testing of autonomous operation of an inverter-based microgrid," *IEEE Trans. Power Electron.*, vol. 22, no. 2, pp. 613−625, Mar. 2007.

[11] P. Kundur, *Power System Stability and Control*. New York, NY, USA: McGraw-Hill, 1994.

[12] H. Xin, L. Huang, L. Zhang, Z. Wang, and J. Hu, "Synchronous instability mechanism of P-f droop-controlled voltage source converter caused by current saturation," *IEEE Trans. Power Syst.*, vol. 31, no. 6, pp. 5206−5207, Nov. 2016.

[13] L. Huang, H. Xin, Z. Wang, L. Zhang, K. Wu, and J. Hu, "Transient stability analysis and control design of droop-controlled voltage source converters considering current limitation," *IEEE Trans. Smart Grid*, vol. 10, no. 1, pp. 578−591, Jan. 2019.

[14] X. Yu, F. Gao, and G. Ding, "Deep learning based transient stability assessment for grid-connected inverter," in *Proc. IEEE International Power Electronics and Application Conference and Exposition (PEAC)*, Shenzhen, China, Nov. 2018.

[15] H. Wu and X. Wang, "Design-oriented transient stability analysis of grid-connected converters with power synchronization control," *IEEE Trans. Ind. Electron.*, vol. 66, no. 8, pp. 6473−6482, Aug. 2019.

[16] L. Zhang, L. Harnefors, and H.-P. Nee, "Power-synchronization control of grid-connected voltage-source converters," *IEEE Trans. Power Syst.*, vol. 25, no. 2, pp. 809−820, May 2010.

[17] L. Zhang, L. Harnefors, and H.-P. Nee, "Interconnection of two very weak AC systems by VSC-HVDC links using power-synchronization control," *IEEE Trans. Power Syst.*, vol. 26, no. 1, pp. 344−355, Feb. 2011.

[18] D. Pan, X. Ruan, C. Bao, W. Li, and X. Wang, "Magnetic integration of the *LCL* filter in grid-connected inverters," *IEEE Trans. Power Electron.*, vol. 29, no. 4, pp. 1573− 1578, Apr. 2014.

[19] D. Pan, X. Ruan, and X. Wang, "Direct realization of digital differentiators in discrete domain for active damping of *LCL*-type grid-connected inverter," *IEEE Trans. Power Electron.*, vol. 33, no. 10, pp. 8461−8473, Oct. 2018.

[20] D. Pan, X. Ruan, X. Wang, F. Blaabjerg, X. Wang, and Q. Zhou, "A highly robust single-loop current control scheme for grid-connected inverter with an improved *LCCL* filter configuration," *IEEE Trans. Power Electron.*, vol. 33, no. 10, pp. 8474−8487, Oct. 2018.

[21] H. Yuan, X. Yuan, and J. Hu, "Modeling of grid-connected VSCs for power system small-signal stability analysis in DC-link voltage control timescale," *IEEE Trans. Power Syst.*, vol. 32, no. 5, pp. 3981−3991, Sep. 2017.

[22] S. H. Strogatz, *Nonlinear Dynamics and Chaos: With Applications to Physics, Biology, Chemistry, and Engineering*, 2nd ed. Boca Raton, FL, USA: CRC Press, 2018.

[23] B. Kroposki, B. Johnson, Y. Zhang, V. Gevorgian, P. Denholm, B.-M. Hodge, and B. Hannegan, "Achieving a 100% renewable grid: operating electric power systems with extremely high levels of variable renewable energy," *IEEE* Power *Energy Mag.*, vol. 15, no. 2, pp. 61−73, Mar./Apr. 2017.